Environmental Science and Pollution Research (2019) 26:11730–11742
https://doi.org/10.1007/s11356-019-04579-3

RESEARCH ARTICLE

Characteristics of single atmospheric particles in a heavily polluted urban area of China: size distributions and mixing states

Li Li[1] · Qiyuan Wang[1,2] · Xu Zhang[3] · Yuanyuan She[4] · Jiamao Zhou[1] · Yang Chen[5] · Ping Wang[6] · Suixin Liu[1] · Ting Zhang[1] · Wenting Dai[1] · Yongming Han[1] · Junji Cao[1,2,7]

Received: 14 September 2018 / Accepted: 13 February 2019 / Published online: 27 February 2019

Abstract
To investigate the chemical composition, size distribution, and mixing state of aerosol particles on heavy pollution days, single-particle aerosol mass spectrometry was conducted during 9–26 October 2015 in Xi'an, China. The measured particles were classified into six major categories: biomass burning (BB) particles, K-secondary particles, elemental carbon (EC)–related particles, metal-containing particles, dust, and organic carbon (OC) particles. BB and EC-related particles were the dominant types during the study period and mainly originated from biomass burning, vehicle emissions, and coal combustion. According to the ambient air quality index, two typical episodes were defined: clean days (CDs) and polluted days (PDs). Accumulation of BB particles and EC-related particles was the main reason for the pollution in Xi'an. Most types of particle size were larger on PDs than CDs. Each particle type was mixed with secondary species to different degrees on CDs and PDs, indicating that atmospheric aging occurred. The mixing state results demonstrated that the primary tracers were oxidized or vanished and that the amount of secondary species was increased on PDs. This study provides valuable information and a dataset to help control air pollution in the urban areas of Xi'an.

Keywords Single particle · Chemical composition · Size distribution · Mixing state · SPAMS · Biomass burning

Responsible editor: Constantini Samara

Electronic supplementary material The online version of this article (https://doi.org/10.1007/s11356-019-04579-3) contains supplementary material, which is available to authorized users.

✉ Qiyuan Wang
wangqy@ieecas.cn

✉ Junji Cao
cao@loess.llqg.ac.cn

[1] Key Laboratory of Aerosol Chemistry and Physics, State Key Laboratory of Loess and Quaternary Geology, Institute of Earth Environment, Chinese Academy of Sciences, Xi'an 710075, China

[2] CAS Center for Excellence in Quaternary Science and Global Change, Xi'an 710061, China

[3] Xi'an Environmental Monitor Station, Xi'an 710061, China

[4] Xi'an Thermal Power Research Institute Co., Ltd., Xi'an 710032, China

[5] Chongqing Institute of Green and Intelligent Technology, Chinese Academy of Sciences, Chongqing 400714, China

[6] Hainan Tropical Ocean University, Sanya 572022, China

[7] Institute of Global Environmental Change, Xi'an Jiaotong University, Xi'an 710049, China

Introduction

High loadings of particulate matter (PM) can influence air quality, human health, and the regional and global climate (Cao 2012; Wang et al. 2014a; Baumer et al. 2008; Lohmann and Feichter 2005; Pöschl 2006; Squizzato et al. 2017). China has suffered from severe air pollution in recent decades due to the rapid industrialization and urbanization (Bi et al. 2015; Liu et al. 2016; He et al. 2016). Xi'an, located in the northwest of China, is not only the economic and cultural center of the northwest region but also one of the world's four great ancient capitals of civilization. With a rapid growth in population and transportation, Xi'an is also facing dire PM pollution problems (Cao et al. 2012b; Chen et al. 2016; Wang et al. 2016a).

Information on the chemical composition of particles is vital to tracing the sources of PM, and a direct relationship exists between particle size and chemical composition (Chen et al. 2014; Healy et al. 2013). Numerous studies have been conducted to characterize the physicochemical properties, sources, and atmospheric processing of aerosol particles in

Xi'an (Chen et al. 2016; Wang et al. 2013; Wang et al. 2017; Wang et al. 2014b). Filter-based analysis has been the main method of studying PM in Xi'an. For example, Wang et al. (2015) analyzed samples of $PM_{2.5}$ filters from different sites in Xi'an and discovered that the loaded $PM_{2.5}$ had eight sources, including coal combustion, motor vehicles, and biomass burning. Zhang et al. (2015) shows that secondary aerosol formation is crucial to haze formation and that relative humidity and stagnant meteorological conditions promote aqueous transformation and increase the loadings of secondary aerosol during haze periods. Traditional offline measurement techniques generally collect samples on filters, which is time-consuming, and potentially decay or degeneration of the chemical species in filters may occur during their transport and storage (Liu et al. 2016). Therefore, a real-time or online measurement tool is urgently launched to investigate the properties of atmospheric aerosols.

Single-particle aerosol mass spectrometry (SPAMS) can provide real-time information on the chemical composition and mixing state of single particle (Cahill et al. 2012; Sultana et al. 2017; Sun et al. 2013; Laskin et al. 2012; Zhang et al. 2014; Yan et al. 2018). Several studies employing SPAMS have been performed in Chinese cities such as Shanghai (Huang et al. 2013; Zhang et al. 2014; Mu et al. 2013; Yang et al. 2012), Guangzhou (Bi et al. 2015, 2011; Zhang et al. 2015), and Beijing (Li et al. 2014; Liu et al. 2016). These studies are beneficial for deep understanding the chemical composition, sources, and mechanism of atmospheric processing of aerosol particles. Studies on single particles have shown the presence of numerous types of particle with complex mixing states in urban areas (Zhang et al. 2013; Hu et al. 2018). The physicochemical properties (e.g., chemical composition, size, and mixing state) of these particle types are unique and influenced by various factors including meteorological conditions and emission sources (Zelenyuk et al. 2008a; Moffet and Prather 2009). Therefore, the behaviors of these particle types in the atmosphere were different; this probably contributes to their distinct effects on the environment and climate.

SPAMS has been employed to study single particles produced by biomass burning, organic particles, and the mixing states of secondary species (Xu et al. 2017; Li et al. 2014; Zhang et al. 2013, 2015). However, the variability of single particles and the mixing states of secondary species with different particle types during heavy pollution events in Xi'an have been rarely reported. In this study, SPAMS was used during October 2015 to characterize the physical and chemical properties of single atmospheric particles in Xi'an. We analyzed the mass spectral and size distributions of single-particle species during pollution periods. This thorough investigation of the different mass spectrum signatures, possible sources of different particle types, and the mixing states of secondary species will improve the understanding of haze formation and evolution in Xi'an.

Methodology

Study site

The largest city in northwest China, Xi'an is located on the Guanzhong Plain at the southern edge of the Loess Plateau. The resident population of Xi'an is more than eight million. Because of rapid economic development and urbanization over past decades, Xi'an has been suffering from serious PM pollution (Cao et al. 2012c; Shen et al. 2011). An intensive single-particle aerosol measurement campaign was implemented during 9–26 October 2015 on the roof (approximately 10 m above ground level) of the Institute of Earth Environment, Chinese Academy of Sciences (34.23° N, 108.88° E). This site is located in a residential area in the southwest of downtown Xi'an (Fig. S1). To the east is Fenghui South Road (approximately 55 m), on which the traffic is moderate, whereas to the south is Keji Yi Road (approximately 20 m), which has less traffic.

SPAMS and data analysis

Particles were measured using a single-particle aerosol mass spectrometer (SPAMS 0515 Model, Hexin Analytical Instrument Co., Ltd., Guangzhou, China). Ambient air was drawn into the spectrometer at a flow rate of 75 mL min^{-1} using a conductive silicone tube with an inner diameter of 6 mm and length of approximately 1 m. The particles were dried using a silica gel tube before entering the spectrometer to prevent condensation of water vapor in the sampling line. A $PM_{2.5}$ cyclone (URG Corp., USA) was installed to exclude coarse particles. An additional pump was employed to shorten the residence time of air in the sampling tube. The principle of SPAMS was described in detail previously (Li et al. 2011). Briefly, particles 0.2–2.0 μm in size are effectively drawn into the vacuum system through a ~0.1-mm critical orifice resulting from a pressure drop from ~760 to 2.2 Torr. The particles were then focused and accelerated to specific velocities on the basis of their aerodynamic diameters, which were determined by two orthogonally orientated continuous neodymium/yttrium aluminum garnet (Nd:YAG) diode laser ($\lambda = 532$ nm) separated by a fixed 6-cm distance. Subsequently, the particles were desorbed/ionized at the source region by a pulsed 266-nm Nd:YAG laser. Positive and negative ions were identified simultaneously by the time-of-flight mass spectrometer. In this study, the energy of the desorption/ionization laser was 0.58 ± 0.023 mJ per pulse, which can produce an energy density of 1.06×10^8 W cm^{-2}. Before sampling was performed, a series of standard polystyrene latex spheres (TSI Inc., Knoxville, TN, USA) of known diameters (0.23, 0.32, 0.51, 0.73, 0.96, 1.4, and 2.0 μm) was used to calibrate the measurement of particle aerodynamic diameter. Positive and negative mass spectra were calibrated using lead nitrate and sodium iodide, respectively.

SPAMS converts all acquired mass spectra into a list of peaks at given mass-to-charge ratios (*m/z*) using several related calculation formulas. The obtained spectral peaks of each single particle subsequently analyzed using YAADA 2.1 (http://www.yaada.org), which is a MATLAB-based software toolkit (version 2012a), for further processing of particle sizes and chemical components. A detailed description of an adaptive resonance theory-based neural network algorithm (ART-2a) is given by Song et al. (1999). Briefly, each particle is first compared to all the peaks of area and *m/z*. If the particles' peaks of area and *m/z* meet the vigilance criterion, these particles are of a similar type. The software repeatedly searches for a particle's area and *m/z* to determine if particles have similar mass spectra. The analysis will be complete once the network has performed a given number of iterations. In this study, a vigilance factor of 0.8, learning rate of 0.05, and 20 iterations were set during data processing. A total of 1,120,797 mass spectra out of 4,906,525 sized particles with size ranging from 0.2 to 2.0 μm were obtained by SPAMS during the whole sampling period. Using ART-2a, 930 clusters out of 2534 clusters were obtained by ART-2a and manually merged into six major classes for further analysis. Each particle cluster was named by the major ion pattern in the positive and negative mass spectra.

Complementary data

Air quality index (AQI), $PM_{2.5}$ mass concentration, temperature, and relative humidity (RH) data were derived from the Online Detection and Analysis Platform of Chinese Air Quality (www.aqistudy.cn). Wind speed (WS) and wind direction (WD) data were collected from Weather Underground (www.wunderground.com).

Results and discussion

Overview

The hourly variation of the $PM_{2.5}$ mass concentration, AQI, total particle counts, and meteorological conditions during the entire campaign period are displayed in Fig. 1. According to the Technical Regulation on the Ambient Air Quality Index (on trial) (HJ633-2012; Table S1), two typical sampling periods were identified: clean days (CDs), corresponding to 9–13 October (AQI < 100), and polluted days (PDs), corresponding to 14–22 October (AQI > 100).

For PDs, high values of AQIs and $PM_{2.5}$ were observed frequently, and the highest AQI (231) and $PM_{2.5}$ mass concentration (181 ± 38 μg m^{-3}) occurred on 20 October at 13:00. The particle count was higher on PDs than CDs. As illustrated in Fig. S2, the total particle count measured using SPAMS was strongly positively correlated with the $PM_{2.5}$ loading on CDs ($r = 0.81$), but no correlation was discovered on PDs ($r = 0.12$). This may be attributed to the limit of the SPAMS detection rate. Given a certain SPAMS detection velocity, because the particle number is much greater on PDs than CDs, numerous particles may go undetected.

As shown in Fig. 1, the diurnal cycles of temperature and RH show a regular anti-correlation throughout the sampling period. On CDs, the RH was relatively low, with an average of 57%. The winds were mainly from the northwest, and the average WS was 2.1 m s^{-1}, with a maximum value of 5.0 m s^{-1}. The meteorological conditions were conducive to the dispersion of pollutants, leading to a low $PM_{2.5}$ mass concentration (35.3 μg m^{-3}) on CDs. On PDs, the winds were mainly blowing from the east and had low WS (1.6 m s^{-1}), which favored pollutant accumulation. Moreover, the RH (72%) was elevated, which promoted the formation of secondary aerosols through aqueous reactions (Sullivan et al. 2009; Chen et al. 2016). Therefore, the $PM_{2.5}$ loadings accumulated and increased, with an average concentration of 106 μg m^{-3}. The sudden decrease in $PM_{2.5}$ concentration on 23 October was caused by precipitation, which results in a scavenging effect on particles. Overall, meteorological conditions were discovered to play a crucial affect in pollution formation.

Classification and mass spectrum characteristics

The average positive and negative mass spectra of the six clusters of particles are collected and shown in Fig. 2 during the sampling period, and the number fraction of each group is summarized in Table 1. Groups were identified on the basis of their chemical characteristics and with reference to the particle types identified in published articles.

1.K-secondary particles This particle type has a positive mass spectrum with strong K^+ peaks ($m/z = 39, 41$) and a negative mass spectrum with strong nitrate ($m/z = -46, -62$) and sulfate ($m/z = -80, -97$) peaks. This particle type has been commonly found in research (e.g., Chen et al. 2016, 2017). Bi et al. (2011) indicated that the positive spectra of K-secondary particles usually contain strong potassium signals, and the negative spectra contain strong sulfate and nitrate signals. Chen et al. (2017) also discovered that the spectra of this group have remarkable signals of potassium, sulfate, and nitrate but weak signals for organic fragment ions in positive spectra.

2.BB particles The average mass spectrum of BB particles contains strong K^+ and Na^+ signals and moderate signals of C_n^+ (such as $m/z = \pm 24, \pm 36, \pm 48, \pm 60$), $C_nH_m^+$ (such as $26[C_2H_2]^+$, $29[C_2H_3]^+$, $39[C_3H_3]^+$, $43[C_3H_7]^+$, $55[C_4H_7]^+$, $57[C_4H_9]^+$), $97[HSO_4]^-$, $80[SO_3]^{2-}$, $62[NO_3]^-$, $46[NO_2]^-$,

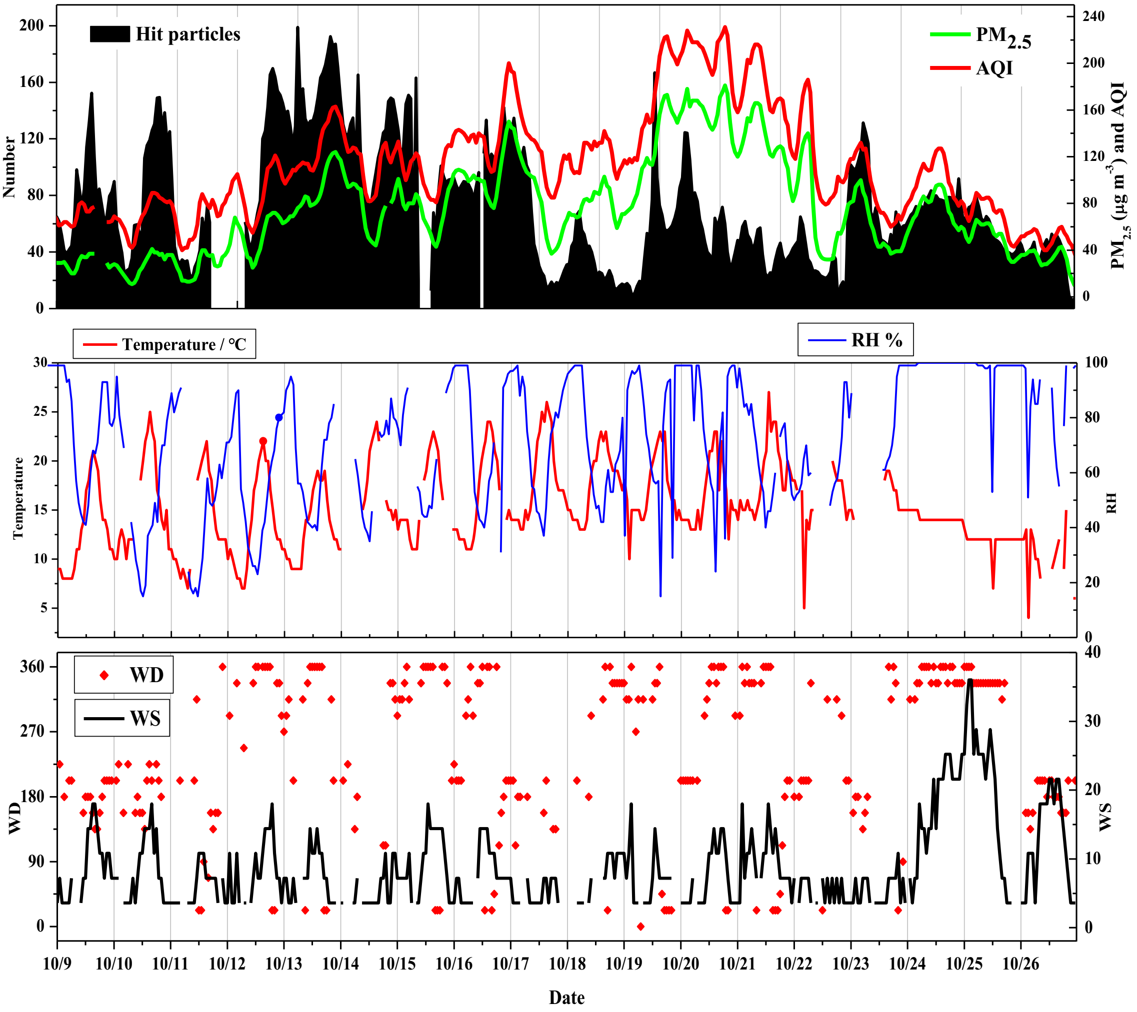

Fig. 1 Temporal profiles (in 1-h resolution) of $PM_{2.5}$ and visibility and meteorological parameters, including temperature, relative humidity (RH), wind direction (WD), and wind speed (WS), during 9–26 October 2015

42[CNO]$^-$, 35, 37[Cl]$^-$, and 26[CN]$^-$, which are consistent with previously reported identification criteria for BB particles (Chen et al. 2016, 2017; Healy et al. 2010). Although potassium is a marker of BB particles, the instrument employed was extremely sensitive to K$^+$ (Gross et al. 2000). Thus, ion fragments of levoglucosan (e.g., 45[CHO]$^{2-}$, 59[C_2H_3O]$^{2-}$, and 71[C_3H_3O]$^-$), CNO$^-$, and CN$^-$ should also be observed simultaneously to identify BB particles (Silva et al. 1999; Bi et al. 2011). Two types of BB particle were identified: aged BB particles (BB-aged) and freshly emitted BB particles (BB-fresh). The spectrum of BB-aged particles had considerably stronger signals for nitrate and 18[NH_4]$^+$ than that of BB-fresh particles; however, the signals for levoglucosan, CNO$^-$, CN$^-$, and Cl$^-$ were weaker on PDs than CDs. The larger signal for 18[NH_4]$^+$ and smaller signal for levoglucosan in BB-aged particles indicate that such particles may be transformed from fresh BB particles when these fresh particles absorb volatile matter and soluble gases during atmospheric aging processes (Pratt et al. 2011; Zauscher et al. 2013).

3.Metal-containing particles Particles containing strong signals for metals (e.g., ^{51}[V]$^+$, ^{52}[Cr]$^{2+}$, ^{54,56}[Fe]$^{2+}$, ^{55}[Mn]$^{2+}$, ^{63,65}[Cu]$^{2+}$, ^{64,66,68}[Zn]$^{2+}$, and ^{206,207,208}[Pb]$^{2+}$) and their oxides are defined as metal-containing particles. As shown by the number fractions listed in Table 1, Fe-, Pb-, and V-containing particles contributed higher proportions (13.9–56.3%) to the total number of metal-containing particles than other metal types (0.7–2.2%). Moreover, minor amounts of Zn, Mn, Cu, and Fe were present in the form of hybrid molecules with Pb on CDs (0.6–7.3%) and PDs (0.5–3.7%). The negative mass spectrum of the metal-containing particles has strong signals of mainly nitrate and sulfate. However, some Fe-containing particles have silicate and phosphate signals in the negative mass spectrum, and the spectrum of Pb-containing particles has a strong signal for nitrate but a weak signal for sulfate. Pb-containing particles have also been observed in other urban areas of China (e.g., Beijing, Shanghai, and Guangzhou) and are considered to originate from fossil fuel

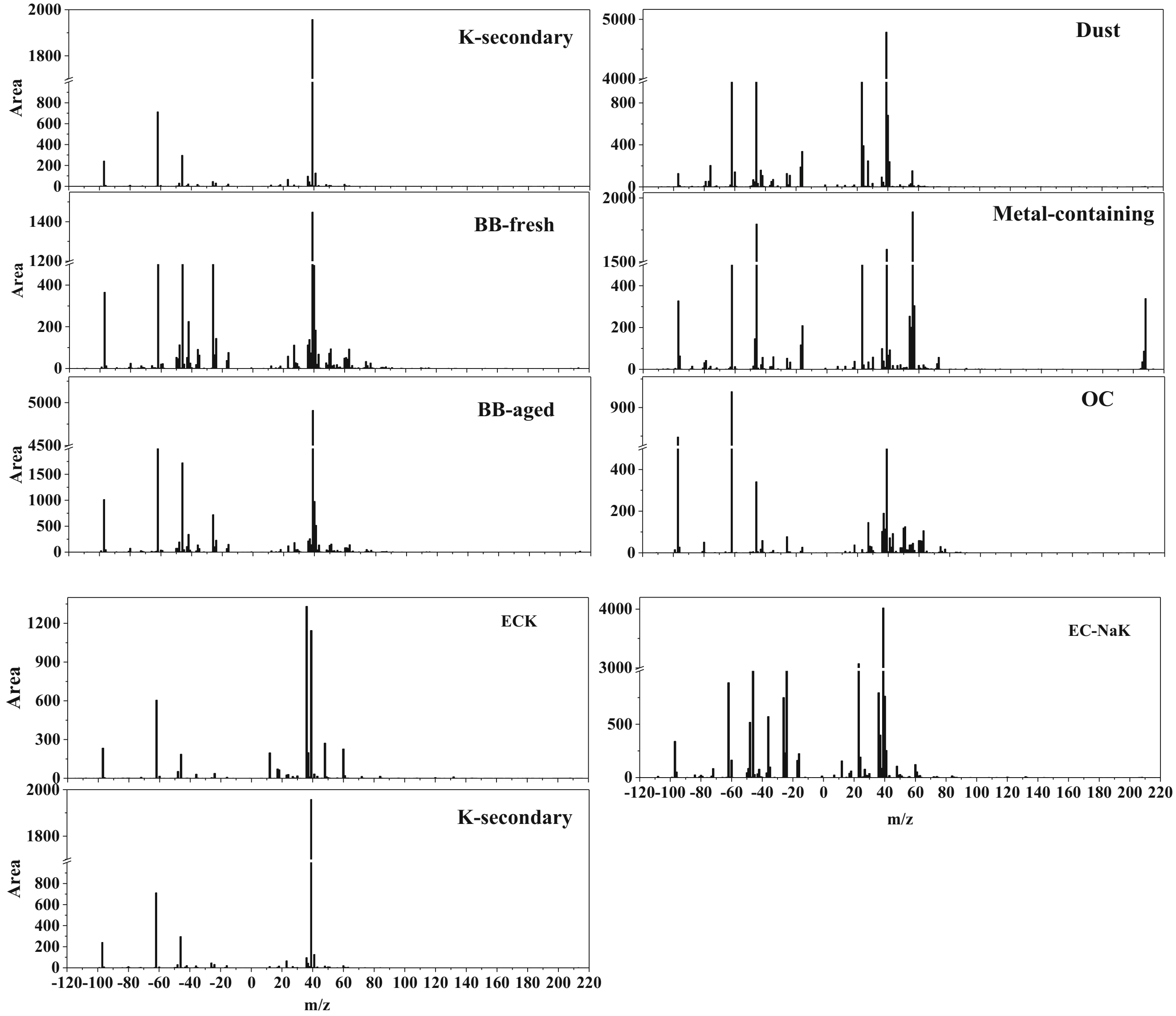

Fig. 2 Average mass spectra of K-secondary, BB-fresh, BB-aged, dust, metal-containing, OC, ECK, EC–NaK, and ECOC particles during the sampling periods

combustion, industrial processes, and waste incineration (Zhang et al. 2009; Ma et al. 2016). Furthermore, atmospheric Pb may serve as a tracer of local emission sources. Pb–Zn–Cl and Pb–Zn–K–Na particles could be associated with waste incineration (Moffet et al. 2008b) and steel manufacturing (Reinard et al. 2007). V-containing particles are a signature of heavy fuel oil combustion (Zauscher et al. 2011; Healy et al. 2009) and may be emitted from heavy trucks at night. The internally mixed ECOC and Pb (ECOC-Pb) particles may be influenced by anthropogenic activities (Bi et al. 2015; Ma et al. 2016).

4.Dust Particles with obvious signals of $40[Ca]^{2+}$, $56[CaO]^{+}$, $79[PO_3]^{-}$, and $76[SiO_3]^{-}$ are classified as dust particles. It should be noted that CaO^{+} and Fe^{2+} both have $m/z = 56$; they are distinguished by whether the signal corresponds to Fe isotope ($m/z = 54$) and $FeOH^{+}$ ($m/z = 73$) or calcium ($m/z = 40$) and $CaOH^{+}$ ($m/z = 57$) (Silva et al. 2000). The typical m/z signal peaks of other crustal element oxides (e.g., $16[O]^{-}$, $17[OH]^{-}$, $24[Mg]^{2+}$, $27[Al]^{3+}$, and $56[Fe]^{2+}$), organic fragments (e.g., $43[C_2H_3O]^{+}$), and C_n^{+} are observed in the average mass spectra of dust particles, and the ion fragments of Cl^{-}, CN^{-}, CNO^{-}, C_n^{-}, nitrate, and sulfate are present in the negative mass spectrum. Fugitive dust is abundant in Xi'an because of the city's geographical location and dry weather (Cao et al. 2013). Fe-containing particles may originate from dust or industrial emissions. If the spectrum of Fe-containing particles contains signals of silicate and phosphate, these particles can be classified as dust;

Table 1 Number fraction of single-particle classes during the campaign

Class	Number 1[a]			Fraction[b] in total (%)			Subtypes	Number 2[a]			Fraction in class (%)		
	WT[c]	CDs[d]	PDs[e]	WT	CDs	PDs		WT	CDs	PDs	WT	CDs	PDs
K-secondary	84,616	17,865	84,416	7.9%	6.8%	12.4%	K-containing	84,359	13,041	70,945	7.9%	5.0%	10.4%
							NaK	257	4824	13,471	0.0%	1.8%	2.0%
BB	458,917	159,033	220,928	43.1%	60.7%	32.4%	BB-aged	439,905	127,823	208,617	41.3%	48.8%	30.6%
							BB-fresh	19,012	31,210	12,311	1.8%	11.9%	1.8%
EC-related	402,750	52,309	288,799	37.8%	20.0%	42.3%	EC–NaK	60,516	15,761	38,306	5.7%	6.0%	5.6%
							ECOC	159,316	26,486	105,679	15.0%	10.1%	15.5%
							ECK	182,918	10,062	144,814	17.2%	3.8%	21.2%
OC	38,258	9841	29,201	3.6%	3.8%	4.3%					Fraction in class (%)		
Metal-containing	31,220	8280	20,307	2.9%	3.2%	3.0%	Fe-containing	17,586	2821	11,685	56.3%	34.1%	57.5%
							Pb-containing	6729	997	3964	21.6%	12.0%	19.5%
							V-containing	4349	1228	2439	13.9%	14.8%	12.0%
							Cu-containing	676	410	–	2.2%	5.0%	–
							Mn-containing	461	238	510	1.5%	2.9%	2.5%
							Sc-containing	–	–	325	–	–	1.6%
							ECOC–Pb	1199	1482	107	4.0%	21.8%	0.5%
							Zn–Pb	–	606	104	–	7.3%	0.5%
							Mn–Pb	–	47	–	–	0.6%	–
							Cu–Pb	–	91	328	–	1.1%	1.6%
							Fe–Pb	–	–	742	–	–	3.7%
							Zn-containing	220	360	103	0.7%	4.3%	0.5%
Dust	48,971	14,541	38,756	4.6%	5.6%	5.7%	Fe-containing	26,378	4232	17,528	53.9%	29.1%	45.2%
							Silicate	10,570	5404	8535	21.6%	37.2%	22.0%
							Ca-containing	10,754	4018	9748	22.0%	27.6%	25.2%
							Mg-containing	789	260	1721	1.6%	1.8%	4.4%
							Al-containing	480	627	1224	1.0%	4.3%	3.2%

[a] Number concentration of particles

[b] Number fraction—the percentage of particles in the corresponding category during the sampling period

[c] Over the entire sampling period

[d] On clean days (CDs)

[e] On pollution days (PDs)

otherwise, they are defined as metal-containing particles (Dall'Osto et al. 2016).

5.Elemental carbon–related particles Particles that have positive or negative mass spectra with clear *m*/*z* for $C_n^{\pm}$ are defined as elemental carbon (EC)–related particles. Although EC particles are chemically inert in the atmosphere, they easily act as a core attracting organic or primary inorganic particles during aging processes. Thus, EC ion fragments can be divided into several types, mainly ECK, EC–NaK ECOC, and minor fresh EC particles (Zhang et al. 2013). Notably, unlike that of pure EC particles, the spectrum of fresh EC has weak ion peaks of organic carbon (OC) and sulfate.

6.Organic carbon particles The signals of OC particles in their positive mass spectrum mainly include those corresponding to various hydrocarbon ion fragments of $C_nH_m^+$ (e.g., $m/z = 27[C_2H_3]^+$, $29[C_2H_3]^+$, $39[C_3H_3]^+$, $43[C_3H_7]^+/[C_2H_3O]^+$, $55[C_4H_7]^+$, and $57[C_4H_9]^+$) and aromatic species (e.g., $m/z = 51[C_4H_3]^+$, $63[C_5H_3]^+$, $77[C_6H_5]^+$, and $91[C_7H_7]^+$). The OC particle mass spectrum obtained in this study is similar to that presented in previous studies. For example, Dall'Osto and Harrison (2012) discovered signatures of cations ($m/z =$ 27, 29, 43, 51, 57, and 63) in the positive spectrum of organic fragments. Wang et al. (2015) identified $27[C_2H_3]^+$ and $43[C_2H_3O]^+$ as the major OC peaks, and the median peaks of *m*/*z* at 51, 63, and 77 were attributed to aromatic compounds.

Characteristics of particles during pollution periods

The percentages of each type of particle are summarized in Table 1 and list the different chemical compositions on CDs and PDs. On CDs, BB particles were the largest contributor (60.7%) to the total particles, followed by EC-related particles (20.0%), with all other types of particle together accounting for 18.7%. By contrast, EC-related particles were the largest contributor (42.3%) on PDs, followed by BB particles (32.4%) and K-secondary particles (12.4%), with other types of particles together contributing 12.9%. These results indicate that accumulation of BB and EC-related particles is the main reason for pollution in Xi'an. The diurnal variation of the six particle types is plotted in Fig. 3. The highest number fraction of K-secondary particles was observed at 15:00, which indicates that photochemical oxidation plays a critical role in the evolution of these particles. The number fraction of BB-aged particles peaked at 18:00, which may have been influenced by the cooking activity in the suburbs surrounding Xi'an, where biofuels (e.g., wood and crop residues) are essential household energy sources (Zhu et al. 2012). The increased number of BB particles observed during 16:00–23:00 may be attributed to the accumulation of particles under the low boundary layer at night. The ion fragments of levoglucosan were fewer on PDs than CDs, as revealed by the mass spectrum of BB particles; this may indicate that the parts of BB particles that were levoglucosan, $26[CN]^-$, and $42[CNO]^-$ possibly have decayed or even vanished due to undergoing a series of atmospheric aging processes (Pratt et al. 2011; Li et al. 2014). Alternatively, the detection limitation of SPAMS may have led to fewer ion fragments in this case. For example, Zelenyuk et al. (2008b) demonstrated that thicker secondary coatings on particles can reduce the efficiency of the SPAMS laser for ablating/ionizing core material; Reinard et al. (2007) suggested that secondary species such as sulfate and nitrate are preferentially ionized, masking the presence of other species. BB-fresh particles can be converted into BB-aged particles, and after further aging, parts of these BB-aged particles are merged into K-secondary particles. This partly accounts for the number fraction of K-secondary particles being higher on PDs than CDs and the number fraction of BB particles being lower on PDs.

EC-related particles mainly include ECK (3.8% on CDs versus 21.2% on PDs), ECOC (10.1% versus 15.5%), and EC–NaK (6.0% versus 5.6%). As illustrated in Fig. 3, the number concentrations of ECK and ECOC particles both decreased after 10:00, which is consistent with the superior dispersion conditions after sunrise. By contrast, the diurnal pattern of EC–NaK shows a slightly increasing trend in the afternoon, which indicates different sources of EC–NaK compared with those of ECOC and ECK particles. EC-related particles have multiple sources including biomass burning and fossil fuels (e.g., motor vehicle emissions and coal combustion) (Healy et al. 2011; Wang et al. 2016c). Li et al. (2014) suggested that EC–NaK is likely to originate from local traffic emissions, whereas ECOC may come from both local traffic emissions and biomass burning.

The diurnal variations of the metal-containing and dust particles were similar (Fig. 3). The amount of dust particles began to rise after 08:00 and peaked at 19:00. This diurnal variation was roughly consistent with the pattern of WS. Moreover, the largest value at 19:00 may have been related to resuspension dust caused by rush hour traffic in the evening. Fe-containing particles were present mainly in the metal-containing and dust particles. The diurnal trends for the metal-containing and dust particles were consistent with that of Fe-containing particles, indicating that Fe-containing particles may be a major contributor to metal-containing and dust particles.

SPAMS can determine size for particles of 0.2–2.0 μm, but particles larger than 1.0 μm generally have low transfer efficiency (Li et al. 2014). Figure S3 shows the number size distribution of the sized and hit particles during the

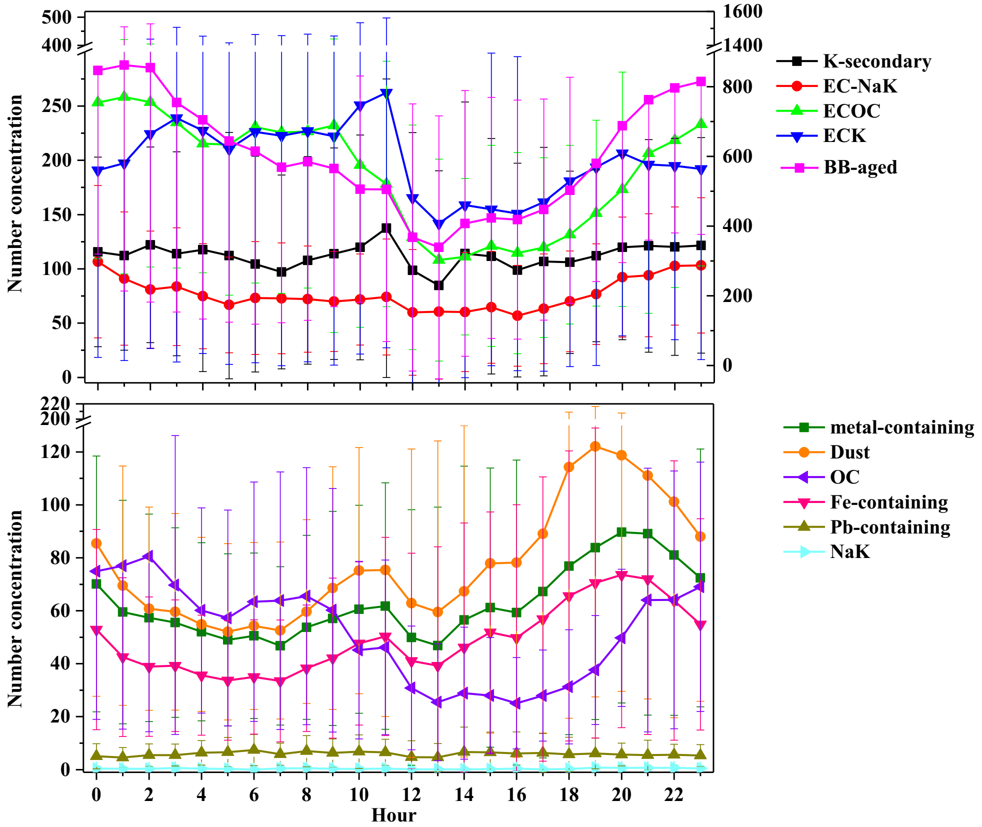

Fig. 3 Diurnal concentration patterns for K-secondary, EC–NaK, ECOC, ECK, BB-aged, metal-containing, dust, OC, Fe-containing, Pb-containing, and NaK particles. The *y*-axis for the BB-aged particle plot is to the right; that for all other particle types is to the left

campaign. Monomodal log-normal distributions were discovered for sized and hit particles, with both having peak values at ~470 nm. The different contributions of each particle type to the size-resolved distribution were identified using the particles' chemical composition and physical properties. As shown in Fig. 4, the particle types is variable with diameters. The distributions of the carbonaceous types (e.g., BB particles, OC, ECOC, and EC) were concentrated mainly in the condensation mode (< 500 nm), whereas droplet mode (> 500 nm) particles were dominated by inorganic types (e.g., metal-containing particles, dust, and NaK). The size distribution of the K-secondary particles on CDs exhibited a slight peak at 350 nm, but on PDs, the peak value was increased to 510 nm. This may be explained by enhanced accumulation during periods of high $PM_{2.5}$ loading leading to the growth of particles. The size distribution of BB particles on PDs shows a peak value at 520 nm, which is slightly larger than that for CDs (500 nm).

The different types of EC-related particles show distinct size distributions. The distributions of EC–NaK, ECOC, and ECK particles are concentrated mainly in the ranges of 500–600, 400–600, and 500–700 nm, respectively, and these particles have larger number fractions on PDs than on CDs. The mass spectral intensities of secondary species (e.g., $18[NH_4]^+$, $43[C_2H_3O]^+$, $62[NO_3]^-$, and $97[HSO_4]^-$) in these types of particles collected on CDs were weak but strong when the particles were collected on PDs, particularly the nitrate and sulfate signals (Fig. 2). ECK and ECOC particles contributed different number fractions to EC-related particles on CDs and PDs. The number fraction of ECK particles sized 500–700 nm was clearly larger for PDs than CDs. Previous studies indicated that a large number of ECK particles in a small size range provide sufficient EC cores for OC formation through the condensation of semivolatile species (Khalizov et al. 2009). Thus, an increase in the number fraction of ECOC was observed on PDs.

The coarse particles collected included dust and metal-containing particles (e.g., Pb and Fe), which had a wider size range—larger than 550–880 nm. This size range is in agreement with particles reported to be present in a suspension of soil dust (Guo et al. 2007). NaK particles represent a minor fraction in the super-micrometer particles, which may reflect crustal element sources (Qin et al. 2012). Fe-containing particles mainly originate from the local iron and steel industry, dust (Dall'Osto et al. 2014; Hu et al. 2018), or fly ash (Zhang et al. 2014).

Mixing state of the particles

The mixing state of primary and secondary species among the major particle types is illustrated in Fig. 5. The criteria for

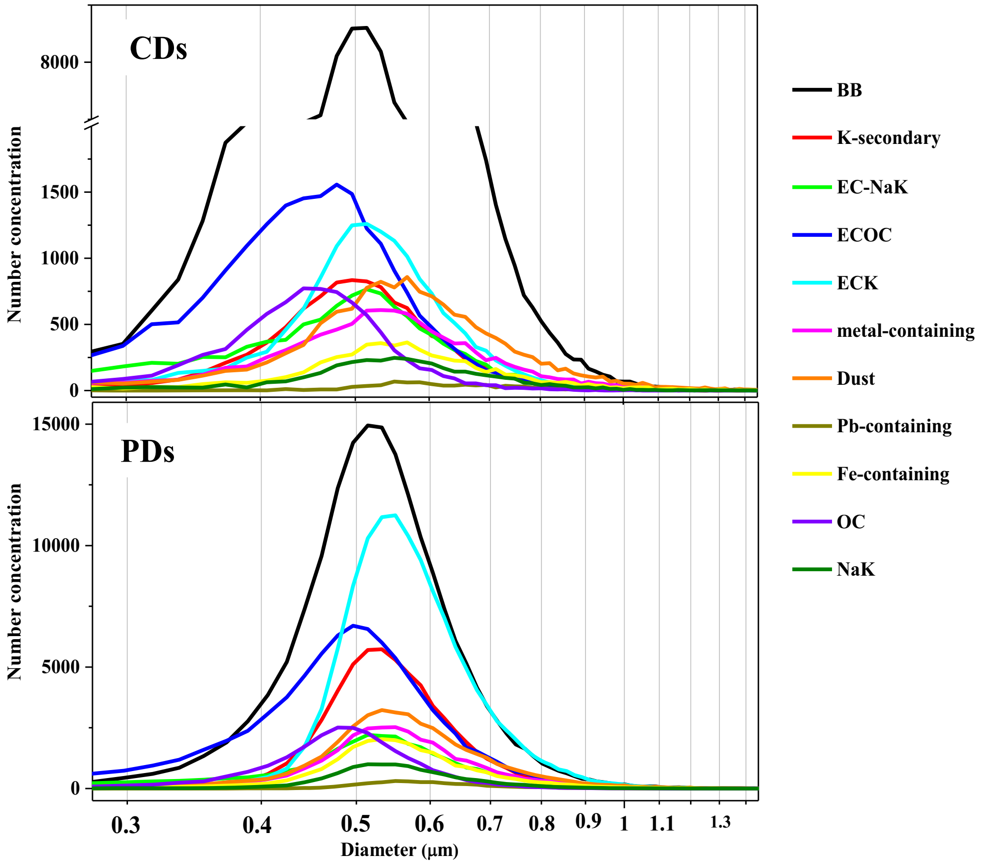

Fig. 4 Size-resolved number concentration of each particle types on CDs and PDs

peak searching in the SPAMS dataset were adopted from those in previous studies (e.g., Silva et al. 1999; Moffet et al. 2008a), and a summary is presented in Table S2. The primary species contained chloride, levoglucosan, cyanide, and silicate, whereas the secondary species included $C_2H_3O^+$, NH_4^+, nitrate, and sulfate. The peaks of *m*/*z* equal to 35, 37$[Cl]^-$ and 113, 115$[K_2Cl]^+$ were selected to reflect the mixing state of chloride in the atmosphere. K_2Cl^+ can be used as a tracer of fresh BB particles because aged BB particles contain more K_2SO_4 and KNO_3. In this study, chloride was mixed mainly with BB-fresh particles (35.5% on CDs versus 54.8% on PDs), BB-aged particles (11.2% versus 5.2%), EC–NaK (37.5% versus 22.8%), ECOC (17% versus 9.6%), Pb (64.3% versus 24.6%), dust (24.6% versus 11.6%), and metal-containing particles (29.1% versus 8.5%). Notably, the lower chloride content of some types of particle (e.g., BB-aged, EC–NaK, ECOC, dust, and metal-containing particles) on PDs than on CDs confirmed that chloride can be removed from the particle phase by the uptake of HNO_3 or H_2SO_4 to form HCl gas during aging processes (Silva et al. 1999; Zauscher et al. 2013).

The *m*/*z* of 45$[CHO_2]^-$, 59$[C_2H_3O_2]^-$, and 71$[C_3H_3O_2]^-$ usually represents the ion fragments of levoglucosan. The number fractions of BB-aged particles mixed with levoglucosan (32.4% on CDs versus 16.9% on PDs) during different periods were smaller than those of BB-fresh particles (61.3% and 69.9%). This may be explained by levoglucosan decaying through atmospheric oxidization processes (Li et al. 2014; Pratt et al. 2011) and the limitation of ionization efficiency of SPAMS under high particulate loadings, which are common for PDs (Reinard et al. 2007; Zelenyuk et al. 2008b). Noticeably, CN was abundant in the BB particles, especially in the BB-fresh particles for both CDs (84.5%) and PDs (99.2%). Meanwhile, the proportion of CN mixed with inorganic matter (e.g., K-containing, NaK, metal-containing particles, and dust) was larger for CDs than PDs; however, the opposite was discovered for the EC-containing particles (e.g., ECK, EC–NaK, and ECOC). The high percentage of carbon-containing particles mixed with CN may have been caused by the presence of both carbon and nitrogen in the particles (Silva et al. 1999).

The *m*/*z* of 60$[SiO_2]^-$ and 76$[SiO_3]^-$ is representative of silicon. The number fractions of dust-related and Fe-containing particles mixed with silicon were 30.9% and 26.6% on CDs and 22.5% and 19.1% on PDs, respectively, indicating that silicon mainly originated from fly ash and mineral dust. The higher proportion of silicon in the metal-containing (21.7% on CDs versus 16.5% on PDs) and EC–NaK (9% versus 7.5%) particles may have been caused by an abundance of silicon particles emitted from coal combustion

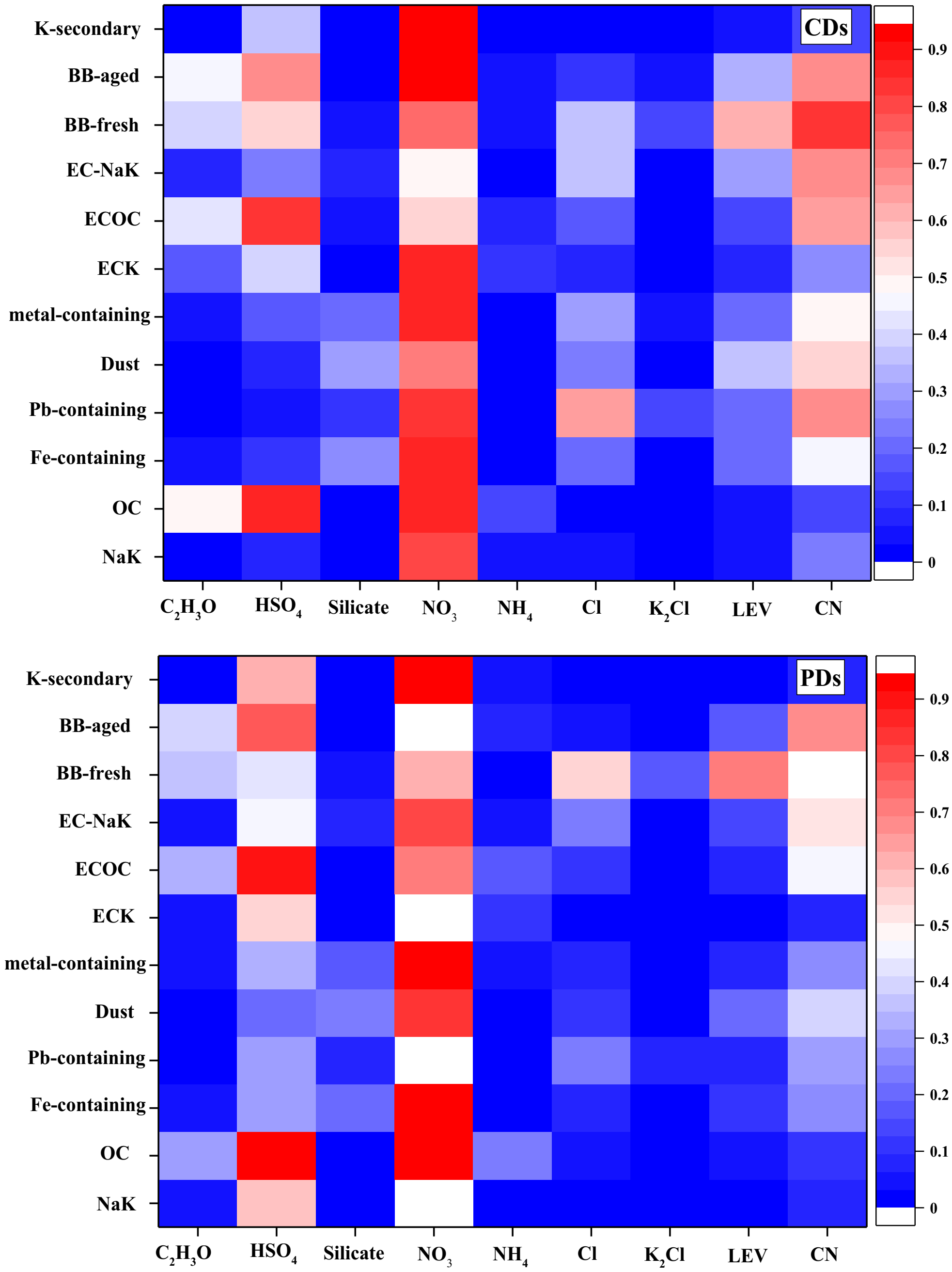

Fig. 5 Mixing state of primary and secondary markers associated with the different particle groups for CDs and PDs, indicated by the coloration. LEV levoglucosan

(Bein et al. 2006). Compared with CDs, the number fraction of silicon in those particle types was lower on PDs, indicating that stagnant weather conditions lead to a decrease in the contribution of dust sources.

The existence of secondary species in different types of particles can provide useful information regarding the chemical processes the particles undergo in the atmosphere. The secondary inorganic species are represented by the markers with *m*/*z* at 18, − 62, and − 97, and the secondary organic species are reflected by *m*/*z* at 43, which can be formed by gas-to-particle conversion or oxidation reactions (Kroll et al. 2012; Ng et al. 2011; Pratt et al. 2011). In this study, ammonium was mainly mixed with 14.3% of OC, 12.0% of ECK, 6.8% of ECOC on CDs and 22.4% of OC, 12.0% of ECK, and 17.7% of ECOC on PDs. Furthermore, more than 40% of the number fractions of BB-aged, OC, and ECOC particles were mixed with $C_2H_3O^+$. Nitrate was found to be abundant in all particles, especially in the inorganic species (> 80%) (e.g., K-secondary, NaK, metal-containing, and dust particles) during the entire campaign, whereas sulfate tends to be mixed with carbonaceous materials (e.g., OC and ECOC). Compared with CDs, the mixing percent of sulfate and carbonaceous particles was more increased on PDs (from 85% of OC and 84% of OCEC on CDs to 92% and 90% on

PDs, respectively), and the proportion of nitrate in inorganic components, such as K-secondary particles (93.3% on CDs versus 93.9% on PDs), NaK (79.8% versus 94.9%), metal-containing particles (87.5% versus 93.4%), and dust (69.8% versus 84.8%) was enhanced. Under polluted environments, SO_2 oxidation leads to high sulfate production rates and promotes the formation of organic matter on aqueous particles (Wang et al. 2016b). Studies have indicated that NH_4^+ tends to neutralize SO_4^{2-} first and then NO_3^- (Hara et al. 1999; Li and Shao 2009). For high $PM_{2.5}$ loading in Xi'an, the NH_4^+ available may not be sufficient to neutralize the SO_4^{2-} and NO_3^- present (Zhang et al. 2011). Under these circumstances, NO_3^- combines with other cations such as Ca^{2+}, Na^+, and K^+.

Conclusions

This study employed SPAMS to investigate the size distributions, compositions, and mixing states of single particles collected in October 2015 in Xi'an, China. CDs and PDs were compared on the basis of the AQI and meteorological conditions. The $PM_{2.5}$ mass concentration was discovered to be 35.3 and 106 μg m^{-3} on CDs and PDs, respectively. A total of 1,120,797 particles were ionized using SPAMS. The ART-2a neural network algorithm was used to classify particle types, and ~96% of the total particles could be clustered into six groups: K-secondary, BB, metal-containing, dust, EC-related particles, and OC particles. BB and EC-related particles were the dominant types on both CDs (60.7%, 20.0%) and PDs (32.4%, 42.3%).

The aging of particles is enhanced under stagnant weather conditions and changes the chemical composition of aerosols, leading to variation in their contributions to the total particles. Weak or absent primary tracers of levoglucosan, Cl, and CN and strong signals of secondary sulfate and nitrate species revealed the increased content of K-secondary and EC-related particles. In general, biomass burning, traffic exhaust, and coal combustion are the possible sources of K-secondary, EC-related, and OC particles. The particles with differing compositions had size dependence. However, most particles were larger on PDs than on CDs due to the particle condensation during aging processes. Clearly, the physical and chemical properties of particles are changed under different pollution conditions. The results of the present study indicate that accumulation of biomass-burning and EC-related particles is the main reason for the pollution in Xi'an. Our study provides clearer understanding of haze formation in the area, especially for those wishing to control pollution effectively in the urban areas of Xi'an.

Funding information This research was supported by the National Natural Science Foundation of China (41503118 and 41661144020) and National Atmospheric Research Program (2017YFC0212200).

References

Baumer D, Vogel BS, Rinke R, Mohler O, Schnaiter M (2008) Relationship of visibility, aerosol optical thickness and aerosol size distribution in an aging air mass over South-West Germany. Atmos Environ 42:989–998

Bein KJ, Zhao YJ, Pekney NJ, Davidson CI, Johnston MV, Wexler AS (2006) Identification of sources of atmospheric PM at the Pittsburgh supersite-part II: quantitative comparisons of single particle, particle number, and particle mass measurements. Atmos Environ 40:424–444

Bi XH, Dai SH, Zhang GH, Qiu N, Li M, Wang XM, Chen DH, Peng PA, Sheng GY, Fu JM (2015) Real-time and single-particle volatility of elemental carbon-containing particles in the urban area of Pearl River Delta region. China Atmos Environ 118:194–202

Bi XH, Zhang GH, Li L, Sheng GY, Fu JM, Zhou Z (2011) Mixing state of biomass burning particles by single particle aerosol mass spectrometer in the urban area of PRD. China Atmos Environ 45:3447–3453

Cahill JF, Suski K, Seinfeld JH, Zaveri RA, Prather KA (2012) The mixing state of carbonaceous aerosol particles in northern and southern California measured during CARES and CalNex 2010. Atmos Chem Phys Discuss 12:10989–11002

Cao JJ, Tie XX, Zhao ZZ, An ZS, Shen ZX, Feng YC (2013) On the potential high acid deposition in northeastern China. J Geophys Res Atmos 118:4834–4846

Cao JJ (2012) Pollution status and control strategies of $PM_{2.5}$ in China. J Earth Environ 3:1030–1036

Cao JJ, Wang QY, Chow JC, Watson JG, Tie XX, Shen ZX, Wang P, An ZS (2012b) Impacts of aerosol compositions on visibility impairment in Xi'an, China. Atmos Environ 59:559–566

Cao JJ, Shen ZX, Chow JC, Watson JG, Lee SC, Tie XX, Ho KF, Wang GH, Han YM (2012c) Winter and summer $PM_{2.5}$ chemical compositions in fourteen Chinese cities. J Air Waste Manag 62:1214–1226

Chen K, Yin Y, Kong SF, Wu YX, Chen JH, Li AH (2014) Size-resolved chemical composition of atmospheric particles during a straw burning period at Mt. Huang (the Yellow Mountain) of China. Atmos Environ 84:380–389

Chen Y, Cao JJ, Huang RJ, Yang FM, Wang QY, Wang YC (2016) Characterization, mixing state, and evolution of urban single particles in Xi'an (China) during wintertime haze days. Sci Total Environ 573:937–945

Chen Y, Wenger JC, Yang FM, Cao JJ, Huang RJ, Shi GM, Zhang SM, Tian M, Wang HB (2017) Source characterization of urban particles from meat smoking activities in Chongqing, China using single particle aerosol mass spectrometry. Environ Pollut 228:92–101

Dall'Osto MB, David CS, Gietl JK, Olatunbosun OA, Yang XG, Harrison RM (2014) Characteristics of tyre dust in polluted air: studies by single particle mass spectrometry (ATOFMS). Atmos Environ 94:224–230

Dall'Osto M, Beddows D, Harrison RM, Onat B (2016) Fine iron aerosols are internally mixed with nitrate in the urban European atmosphere. Environ Sci Technol 50:4212–4220

Gross DS, Gälli ME, Siliva PJ, Prather KA (2000) Relative sensitivity factors for alkali metal and ammonium cations in single-particle aerosol time-of-flight mass spectra. Anal Chem 72:416–422

Guo XY, Zhao WW, Huang MQ, Zheng HY (2007) Single particle analysis of soil dust by aerosol time-of-flight laser mass spectrometry. Opt Appl 37:229–235

Hara K, Osada K, Hayashi M, Matsunaga K, Shibata T, Iwasaka Y (1999) Fractionation of inorganic nitrates in winter Arctic troposphere:

coarse aerosol particles containing inorganic nitrates. J Geophys Res 104:23671–23679

He Q, Zhou G, Geng F, Gao W, Yu W (2016) Spatial distribution of aerosol hygroscopicity and its effect on $PM_{2.5}$ retrieval in East China. Atmos Res 170:161–167

Healy RM, Hellebust S, Kourtchev I, Allanic A (2010) Source apportionment of $PM_{2.5}$ in Cork Harbour, Ireland using a combination of single particle mass spectrometry and quantitative semi-continuous measurements. Atmos Chem Phys 10:9593–9613

Healy RM, O'Connor IP, Hellebust S, Allanic A, Sodeau JR, Wenger JC (2009) Characterization of single particles from in-port ship emissions. Atmos Environ 43:6408–6414

Healy RM, Sciare J, Poulain L, Crippa M (2013) Quantitative determination of carbonaceous particle mixing state in Paris using single particle mass spectrometer and aerosol mass spectrometer measurements. Atmos Chem Phys 13:9479–9496

Healy RM, Sciare J, Poulain L, Kamili K, Merkel M, Müller T, Wiedensohler A, Eckhardt S, Stohl A, Sardaestève R (2011) Sources and mixing state of size-resolved elemental carbon particles in a European megacity: Paris. Atmos Chem Phys 12:1681–1700

Hu R, Wang HL, Yin Y, Zhu B, Xia L, Zhang ZF, Chen K (2018) Measurement of ambient aerosols by single particle mass spectrometry in the Yangtze River Delta, China: seasonal variations, mixing state and meteorological effects. Atmos Res 213:562–575

Huang Y, Li L, Li J, Wang X, Chen H, Chen J, Yang X, Gross DS, Wang H, Qiao L (2013) A case study of the highly time-resolved evolution of aerosol chemical and optical properties in urban Shanghai. China Atmos Chem Phys 13:3931–3944

Khalizov AF, Zhang RY, Zhang D, Xue HX, Pagels J, Mcmurry PH (2009) Formation of highly hygroscopic soot aerosols upon internal mixing with sulfuric acid vapor. J Geophys Res Atmos 114:D5

Kroll JH, Smith JD, Worsnop DR, Wilson KR (2012) Characterization of lightly oxidized organic aerosol formed from the photochemical aging of diesel exhaust particles. Environ Chem 9:211

Laskin A, Laskin J, Nizkorodov SA (2012) Mass spectrometric approaches for chemical characterization of atmospheric aerosols: critical review of the most recent advances. Environ Chem 9:163–189

Li L, Huang ZX, Dong JG, Li M, Gao W, Nian HQ, Fu Z, Zhang GH, Bi XH, Cheng P (2011) Real time bipolar time-of-flight mass spectrometer for analyzing single aerosol particles. Int J Mass Spectrom 303:118–124

Li L, Li M, Huang ZX, Gao W, Nian HQ, Fu Z, Gao J, Chai FH, Zhou Z (2014) Ambient particle characterization by single particle aerosol mass spectrometry in an urban area of Beijing. Atmos Environ 94: 323–331

Li WJ, Shao Y (2009) Observation of nitrate coatings on atmospheric mineral dust particles. Atmos Chem Phys 9:1863–1871

Liu L, Wang YL, Du SY, Zhang WJ, Hou LJ, Vedal S, Han B, Yang W, Chen MD, Bai ZP (2016) Characteristics of atmospheric single particles during haze periods in a typical urban area of Beijing: a case study in October, 2014. J Environ Sci 40:145–153

Lohmann U, Feichter J (2005) Global indirect aerosol effects: a review. Atmos Chem Phys 5:715–737

Ma L, Li M, Huang ZX, Li L, Gao W, Nian HQ, Zou LL, Fu Z, Gao J, Chai FH (2016) Real time analysis of lead-containing atmospheric particles in Beijing during springtime by single particle aerosol mass spectrometry. Chemosphere 154:454–462

Moffet RC, Foy BD, Molina LT, Molina MJ, Prather KA (2008a) Measurement of ambient aerosols in northern Mexico city by single particle mass spectrometry. Atmos Chem Phys 8:4499–4516

Moffet RC, Desyaterik Y, Hopkins RJ, Tivanski AV, Gilles MK, Wang Y, Shutthanandan V, Molina LT, Abraham RG, Johnson KS, Mugica V, Molina MJ, Laskin A, Prather KA (2008b) Characterization of aerosols containing Zn, Pb, and Cl from an industrial region of Mexico city. Environ Sci Technol 42:7091–7097

Moffet RC, Prather KA (2009) In-situ measurements of the mixing state and optical properties of soot with implications for radiative forcing estimates. PNAS 106:11872–11877

Mu YY, Lou SR, Chen CH, Zhou M, Wang HL, Zhou Z, Qiao LP, Huang C, Li M, Li L (2013) Aging and mixing state of particulate matter during aerosol pollution episode in autumn Shanghai using a single particle aerosol mass spectrometer (SPAMS). Environ Sci 34:2071–2080

Ng NL, Canagaratna MR, Jimenez JL, Chhabra PS, Seinfeld JH, Worsnop DR (2011) Changes in organic aerosol composition with aging inferred from aerosol mass spectra. Atmos Chem Phys Discuss 11:6465–6474

Pöschl U (2006) Atmospheric aerosols: composition, transformation, climate and health effects. Cheminform 37:7520–7540

Pratt KA, Murphy SM, Subramanian R, Demott PJ, Kok GL, Campos T, Rogers DC, Prenni AJ, Heymsfield AJ, Seinfeld JH (2011) Flight based chemical characterization of biomass burning aerosols within two prescribed burn smoke plumes. J Phys Society of Jpn 76:45–49

Qin X, Pratt KA, Shields LG, Toner SM, Prather KA (2012) Seasonal comparisons of single-particle chemical mixing state in Riverside, CA. Atmos Environ 59:587–596

Reinard MS, Adou K, Martini JM, Johnston MV (2007) Source characterization and identification by real-time single particle mass spectrometry. Atmos Environ 41:9397–9409

Shen Z, Cao JJ, Liu SX, Zhu CS, Wang X, Zhang T, Xu HM, Hu TF (2011) Chemical composition of PM_{10} and $PM_{2.5}$ collected at ground level and 100 meters during a strong winter-time pollution episode in Xi'an, China. J. Air Waste Manage 61:1150–1159

Silva PJ, Carlin RA, Prather KA (2000) Single particle analysis of suspended soil dust from southern California. Atmos Environ 34: 1811–1820

Silva PJ, Liu DY, Noble CA, Prather KA (1999) Size and chemical characterization of individual particles resulting from biomass burning of local southern California species. Environ Sci Technol 33: 3068–3076

Song XH, Hopke PK, Fergenson DP, Prather KA (1999) Classification of single particles analyzed by ATOFMS using an artificial neural network, ART-2A. Anal Chem 71:860–865

Squizzato S, Cazzaro M, Innocente E, Visin F, Hopke PK, Rampazzo G (2017) Urban air quality in a mid-size city:$PM_{2.5}$ composition, sources and identification of impact areas: from local to long range contributions. Atmos Res 186:51–62

Sultana CM, Collins DB, Prather KA (2017) The effect of structural heterogeneity in chemical composition on online single particle mass spectrometry analysis of sea spray aerosol particles. Environ Sci Technol 51:3660–3668

Sullivan RC, Moore MJK, Petters MD, Kreidenweis MS, Roberts GC, Prather KA (2009) Effect of chemical mixing state on the hygroscopicity and cloud nucleation properties of calcium mineral dust particles. Atmos Chem Phys 9:1887–1893

Sun YL, Wang ZF, Fu PQ, Yang T (2013) Aerosol composition, sources and processes during wintertime in Beijing. China Atmos Chem Phys Discuss 13:4577–4592

Wang GH, Zhou BH, Cheng CL, Cao JJ, Li JJ, Meng JJ, Tao J, Zhang RJ, Fu PQ (2013) Impact of Gobi desert dust on aerosol chemistry of Xi'an, inland China during spring 2009: differences in composition and size distribution between the urban ground surface and the mountain atmosphere. Atmos Chem Phys 13:819–835

Wang K, Han YM, Ho SH, Zhang T, Liu SX, Cao JJ (2017) Comparison of characteristics and reactive oxidative species of $PM_{2.5}$ in Xi'an, China during haze and clean days. Environ Sci 7:2679–2687

Wang Y, Zhang R, Saravanan R (2014a) Asian pollution climatically modulates mid-latitude cyclones following hierarchical modelling and observational analysis. Nat Commun 5:1–7

Wang Q, Lu X, Pan H (2016a) Analysis of heavy metals in the re-suspended road dusts from different functional areas in Xi'an. China Environ Sci Pollut R 23:19838–19846

Wang GH, Zhang RY, Gomez ME, Yang LX, Zamorac ML, Hu M, Lin Y, Peng JF, Guo S, Meng JJ, Li JJ, Cheng CL, Hu TF, Ren YP, Wang YS, Gao J, Cao JJ, An ZS, Zhou WJ, Li GH, Wang JY, Tian PF, Ortiz WM, Secrest J, Du ZF, Zheng J, Shang DJ, Zeng LM, Shao M, Wang WG, Huang Y, Wang Y, Zhu YJ, Li YX, Hu JX, Pan BW, Cai L, Cheng YT, Ji YM, Zhang F, Rosenfeld D, Liss PS, Ducec RA, Kolb CE, Molina MJ (2016b) Persistent sulfate formation from London fog to Chinese haze. PNAS 113:13630–13635

Wang QY, Huang RJ, Zhao ZZ, Cao JJ, Ni HY, Tie XX, Zhao SY, Su XL, Han YM, Shen ZX, Wang YC, Zhang NN, Zhou YQ, Corbin JC (2016c) Physicochemical characteristics of the black carbon aerosol and its radiative impact in a polluted urban area of China. J Geophys Res Atmos 121:12505–12519

Wang QY, Huang RJ, Cao JJ, Han YM, Wang GH, Li GH, Wang YC, Dai WT, Zhang RJ, Zhou YQ (2014b) Mixing state of black carbon aerosol in a heavily polluted urban area of China: implications for light absorption enhancement. Aerosol Sci Technol 48:689–697

Xu J, Li M, Shi G, Wang H, Ma X, Wu J, Shi X, Feng Y (2017) Mass spectra features of biomass burning boiler and coal burning boiler emitted particles by single particle aerosol mass spectrometer. Sci Total Environ 598:341–352

Yan JP, Chen LQ, Zhao SH, Zhang MM, Lin Q, Li L (2018) Impact of marine and continental sources on aerosol characteristics using an on-board SPAMS over southeast sea, China. Environ Sci Pollut Res Int 25(30):30659–30670 Accepted

Yang F, Chen H, Du JF, Yang X, Gao S, Chen JM, Geng FH (2012) Evolution of the mixing state of fine aerosols during haze events in Shanghai. Atmos Res 104-105:193–201

Zauscher MD, Wang Y, Moore MJ, Gaston CJ, Prather KA (2013) Air quality impact and physicochemical aging of biomass burning aerosols during the 2007 San Diego wildfires. Environ Sci Technol 47:7633–7643

Zauscher MD, Moore MJK, Lewis GS, Hering SV, Prather KA (2011) Approach for measuring the chemistry of individual particles in the size range critical for cloud formation. Anal Chem 83:2271–2278

Zelenyuk A, Imre D, Han JH, Oatis S (2008a) Simultaneous measurements of individual ambient particle size, composition, effective density, and hygroscopicity. Anal Chem 80:1401–1407

Zelenyuk A, Yang J, Song C, Zaveri RA, Imre D (2008b) "Depth-profiling" and quantitative characterization of the size, composition, shape, density, and morphology of fine particles with SPLAT, a single-particle mass spectrometer. J Phys Chem A 112:669–677

Zhang GH, Bi XH, Li L, Chan LY, Li M, Wang XM, Sheng GY, Fu JM, Zhou Z (2013) Mixing state of individual submicron carbon-containing particles during spring and fall seasons in urban Guangzhou, China: a case study. Atmos Chem Phys 13:4723–4735

Zhang GH, Bi XH, Lou SR, Li L, Wang HL, Wang XM, Zhou Z, Sheng GY, Fu JM, Chen CH (2014) Source and mixing state of iron-containing particles in Shanghai by individual particle analysis. Chemosphere 95:9–16

Zhang GH, Han BX, Bi XH, Dai SH, Huang W, Chen DH, Wang XM, Sheng GY, Fu JM, Zhou Z (2015) Characteristics of individual particles in the atmosphere of Guangzhou by single particle mass spectrometry. Atmos Res 153:286–295

Zhang T, Cao JJ, Tie XX, Shen ZX, Liu SX, Ding H, Han YM, Wang GH, Ho KF, Qiang J, Li WT (2011) Water-soluble ions in atmospheric aerosols measured in Xi'an, China: seasonal variations and sources. Atmos Res 102:110–119

Zhang YP, Wang XF, Chen H, Yang X, JChen JM, Allen JO (2009) Source apportionment of lead-containing aerosol particles in Shanghai using single particle mass spectrometry. Chemosphere 74:501–507

Zhu JC, Li RH, Zhang ZQ, Liu X, Lv X, Wang GH (2012) The rural household energy consumption structure analysis of Shanxi province. Renew Energy Resour 2